Enhanced optoelectronics performance of hybrid self power photodetectors GO: TiO2- AD / n-Si heterojunctions

Mohammed J. AlSultani

Maysoon F. Alias

University of
Kerbala

Enhanced optoelectronics performance of hybrid self power photodetectors GO: TiO2- AD / n-Si heterojunctions

Abstract

A GO:TiO_2/n-Si heterostructure has been submerged in an anthocyanin dye solution that extracted from the red cabbage plant creates a high responsivity, self-powered UV, and visible photodetectors fabricated by the spray pyrolysis technique. The GO concentrations are varied, whereas TiO_2 is fixed. Thin films' structure, shape, and optical characteristics were examined using X-ray diffraction, field emission scanning electron microscopy, and UV-Vis spectrophotometers respectively. Island-like polycrystalline film powders with grain boundaries and granular shapes are created. Two direct energy gaps between 3.33-3.02 and 2.39-2.04 eV exist in all films. J-V characteristics were examined. The saturation current density (J_o), the ideality factor (n), the barrier height (φ_b), and the resistance (R_s) were estimated using the Cheung methodology and traditional methods. The GO concentration has massively lowered leakage current and the ideality factor. (C-V) properties were computed. As the GO concentration rises, (V_{bi}), (E_F), and φ_b values rise, whereas the effective carrier concentration (N_d) and $\Delta\varphi_b$ values decrease. Capacitance rapidly decreased as reverse voltage rose owing to the broadening of the heterojunction depletion layer led to improve photodetection. The photodetector devices were evaluated at 380−620 nm. These devices showed steady current across numerous cycles and great repeatability and stability. Calculated merit statistics included responsivity (R_λ), specific detectivity (D*), external quantum efficiency (EQE), photosensitivity (ξ), and noise equivalent power (NEP). The greatest values for R_λ, EQE, D* and NEP were 0.96 A.W^{-1} and 305.5%, 3.06×10^{11} cm. $Hz^{1/2}$. W^{-1} and 8.39×10^{-13} W. $Hz^{-1/2}$ at 4: 4 GO: TiO_2-AD/n-Si concentration. GO: TiO_2-AD/n-Si self-power photodetectors have excellent weak light detection, could be considered as an attractive candidates for optoelectronic devices such as hybrid or dye-sensitized solar cells and photodetectors.

Keywords: TiO_2: GO thin films, Anthocyanin dye, Structural properties, Morphological properties, Optical properties, Photodetector, Figure of merit of photodetector

Keywords
Keywords: TiO2: GO thin films, Anthocyanin dye, Structural properties, Morphological properties, Optical properties, Photodetector, Figure of merit of photodetector

Creative Commons License

RESEARCH PAPER

Enhanced Optoelectronics Performance of Hybrid Self Power Photodetectors GO:TiO$_2$-AD/n-Si Heterojunctions

Mohammed J. AlSultani, Maysoon F. Alias[*]

Physics Department, College of Science, University of Baghdad, Jadriya, Baghdad, Iraq

Abstract

A GO:TiO$_2$/n-Si heterostructure has been submerged in an anthocyanin dye solution that extracted from the red cabbage plant creates a high responsivity, self-powered UV, and visible photodetectors fabricated by the spray pyrolysis technique. The GO concentrations are varied, whereas TiO$_2$ is fixed. Thin films' structure, shape, and optical characteristics were examined using X-ray diffraction, field emission scanning electron microscopy, and UV-Vis spectrophotometers respectively. Island-like polycrystalline film powders with grain boundaries and granular shapes are created. Two direct energy gaps between 3.33–3.02 and 2.39–2.04 eV exist in all films. J-V characteristics were examined. The saturation current density (J$_o$), the ideality factor (n), the barrier height (φ_b), and the resistance (R$_s$) were estimated using the Cheung methodology and traditional methods. The GO concentration has massively lowered leakage current and the ideality factor. (C−V) properties were computed. As the GO concentration rises, (V$_{bi}$), (E$_F$), and φ_b values rise, whereas the effective carrier concentration (N$_d$) and $\Delta\varphi_b$ values decrease. Capacitance rapidly decreased as reverse voltage rose owing to the broadening of the heterojunction depletion layer led to improve photodetection. The photodetector devices were evaluated at 380−620 nm. These devices showed steady current across numerous cycles and great repeatability and stability. Calculated merit statistics included responsivity (R$_\lambda$), specific detectivity (D*), external quantum efficiency (EQE), photosensitivity (ξ), and noise equivalent power (NEP). The greatest values for R$_\lambda$, EQE, D* and NEP were 0.96 A·W^{-1} and 305.5%, 3.06 × 10^{11} cm·Hz$^{1/2}$·W^{-1} and 8.39 × 10^{-13} W·Hz$^{-1/2}$ at 4: 4 GO: TiO$_2$-AD/n-Si concentration. GO: TiO$_2$-AD/n-Si self-power photodetectors have excellent weak light detection, could be considered as an attractive candidates for optoelectronic devices such as hybrid or dye-sensitized solar cells and photodetectors.

Keywords: TiO$_2$: GO thin films, Anthocyanin dye, Structural properties, Morphological properties, Optical properties, Photodetector, Figure of merit of photodetector

1. Introduction

Organic materials have been primarily used for photodetectors because of their broad surface area, cost-effectiveness, chemical stability, mechanical flexibility, eco-friendliness, and capability to detect specific wavelengths [1,2]. Among these solid and long-lasting nanostructures, graphene oxide (GO) is a compound made of carbon, oxygen, and hydrogen that shows excellent potential in photodetection because of its high mobility and its high band gap characteristics, since the combination of both insulating sp^3 and conducting sp^2 regions. GO exhibits p-type semiconductor properties [3]. Furthermore, the GO thin film demonstrates outstanding properties in photodetectors, gas sensing, and numerous other applications [4,5]. GO-metal oxide hybrid structures exhibit distinct structural and optoelectronic properties compared to GO, making them highly suitable for detector applications [6,7]. The metal oxide semiconductor inorganic optical detector requires further features to be suitable for commercial use, as it currently exhibits slow switching speed, substantial noise

levels, and high dark current [8,9]. Comparatively, GO-metal oxide heterostructures show better charge separation and reduced charge recombination [10]. Furthermore, the charges at the interface might substantially improve the gadget's performance. Because of this, it is essential to look into different wide-band semiconductor nanostructures to make a heterojunction with silicon. This will make controlling one-color, dual-color, and multi-color photodetection easier [11]. For example, demonstrate that adding GO to titanium dioxide (TiO_2) decreases the optical band gap of the nanocomposite to a value lower than 2.50 eV [12]. Additionally, natural dye sensitizers are crucial to enhancing the efficiency of photodetection.

The characteristics of a substance, such as its absorption spectrum and charge transfer properties, primarily determine how it behaves. Natural dye is readily accessible, simple to manufacture, cost-effective, nontoxic, eco-friendly, and completely biodegradable [13,14]. William et al. [15] found that natural dyes from *B. guineensis* can be used to sensitize TiO_2–GO composite thin films, improving their physical and chemical properties.

The anthocyanin family's presence typically causes their photoactivity [16,17]. Anthocyanin is a pigment that gives fruits, flowers, and leaves a red, blue, or purple color. The absorption spectrum of anthocyanin falls within the visible range of light, specifically between 450 and 580 nm. The dye sensitizer employed can be derived from red cabbage [18]. It can bind to the surface of TiO_2 and transfer electrons to the conduction band of TiO_2 [19,20]. In this study, a low noise, fast responding multi-photodetector of GO:TiO_2-Anthocyanin Dye (AD)/n-Si heterostructure were fabricated using the chemical spray pyrolysis method. This hybrid heterostructure is an exciting choice for detector uses because it is good at separating charges, being responsive, and being sensitive.

2. Experimental details

2.1. Materials

The process involved depositing GO:TiO_2 films onto n-Si substrates using the spray pyrolysis technique and immersed them in anthocyanin dye for 24 h. The Hummer technique is used to produce graphene oxide by mixing 10 g graphite powder, 4 g $NaNO_3$, 6 g $KMnO_4$, and 0.01 g boric acid with 100 ml of concentrated H_2SO_4 in an ice bath at 0−5 °C for 1 h. Gradually, 5 g of $KMnO_4$ was added and stirred at 35 °C for 2 h 50 ml of distilled water was added and stirred at 95 °C for 30 min 12 ml of

H_2O_2 was added and mixed for 30 min at room temperature. The suspension is then centrifuged, washed, and filtered. The graphene oxide is then dehydrated at 40 °C for 24 h. Amounts of 0.05, 0.1, 0.2, 0.3, 0.4, and 0.5 g of graphene oxide were dissolved in 10 ml of acidified ethanol solvent, yielding ratios of 0.5%, 1%, 2%, 3%, 4%, and 5% (w/v), respectively.

The precursor suspension was prepared by combining 6 ml of titanium tetraisopropoxide (TTIP), 1.2 ml of glacial acetic acid, 37 ml of deionized water, and 1 ml of concentrated nitric acid. The solution was agitated for 30 min, so a clear solution is obtained. The mixture was then recondensed at 80 °C for 90 min. 0.4 g of titanium (IV) nanopowder, specifically anatase from Skyspring Nanomaterials, Inc., was added to the suspension with 10 ml of precursor. 250 μl of deionized water and 12 ml of acidic ethanol were added to the mixture, and the solution underwent 10 min of sonication after 15 min of agitation.

The preparation of the anthocyanin process involves chopping 50 g of red cabbage leaves with a mixture of 100 ml of methanol, 50 ml of acetone, and 50 ml of distilled water according to the ratio (2:1:1). The mixture is then placed in a water bath at 50 °C for 1 h. After the time is finished, three drops of HCl are added to the dye extract, and the solution is filtered. The filtered solution is then placed in a rotary evaporator to remove the ethanol, acetone, and distilled water. The dye remains, and the solution is dried in an oven at 60 °C for 24 h. The 0.2 g of desiccated dye is then dissolved in 40 ml of isopropyl alcohol and 3 ml of glacial acetic acid and stirred for 10 min at 70 °C. Finally, 50 μl of HNO_3 acid is added, causing the solution to turn red.

The experiment has been involved mixing different concentrations of GO suspensions: 0.5%, 1%, 2%, 3%, 4%, and 5% (w/v) with a 4% (w/v) TiO_2 suspension. The volume ratios were 0.5:4, 1:4, 2:4, 3:4, 4:4, and 5:4. After stirring for 30 min, the mixtures underwent sonication for 5 min. They were subsequently sprayed onto an n-Si substrate. A diluted hydrofluoric acid (HF) solution with deionized water (1:10) was used to remove the SiO_2 layer already on the substrates before the spray was used. The substrates were then dried after these processes.

2.2. Characterization of GO: TiO_2-AD/n-Si films and photodiodes

Using a Blazer union coating unit (BAE 370 thermal evaporation system) under a vacuum of 10^{-6} mbar, aluminum pure finger-shaped metal contacts were deposited on top of GO:TiO_2-AD/n-Si

thin films as electrodes. The aluminum electrode mask consists of digitized fingers, each measuring 0.2 mm in width and 5 mm in length. The total size of the device is 25 mm^2, which includes an effective transmission area of 16 mm^2. Fig. 1a illustrates the schematic diagram of a cross-section of one side from metal contact on the photodiodes. Structural and surface morphological properties were investigated using PANalytical Aeris XRD and scanning electron microscopy (FESEM, Model Inspect F50). An optical analysis was conducted using a Shimadzu 1900 UV spectrophotometer to examine the optical characteristics. The Keithley 4500 semiconductor characterization equipment and the WK HF LCR Meters 6500 P were used to measure the photodiodes' J-V and C−V characteristics. The study measured the time-dependent photo switching using LEDs emitting light at specific wavelengths: UV at 380 nm, blue at 460 nm, green at 550 nm, and red at 620 nm. The intensity of the LEDs was 6.17 mW/cm^2 for UV, 5.61 mW/cm^2 for blue, 10.38 mW/cm^2 for green, and 5.11 mW/cm^2 for red. The measurements were taken at room temperature without applying any voltage. This can be seen in Fig. 1b.

3. Results and discussion

3.1. Structural and morphological properties

The XRD patterns of GO, TiO$_2$ powders, and GO:TiO$_2$-AD are examined as shown in Fig. 2. The GO produced showed a peak at $2\theta = 11.7°$ (001) plane and a peak at $2\theta = 24.21°$ (002) plane, indicating some of GO was reduced [21]. The diffraction pattern of TiO$_2$ indicates a maximum intensity peak at $2\theta = 25.28°$ in the (101) plane, indicating the anatase phase [22] for tetragonal structure with a = b = 3.77 Å and c = 9.49 Å lattice constants (JCPDS # 00-002-0387). The GO:TiO$_2$ films showed polycrystalline structure and distinct peaks at $2\theta = 24.73°, 25.53°, 36.43°, 46.53°,$ and $53.56°,$ corresponding to planes (002), (101), (004), (200), and (211). The optimum peak is observed at the (101)
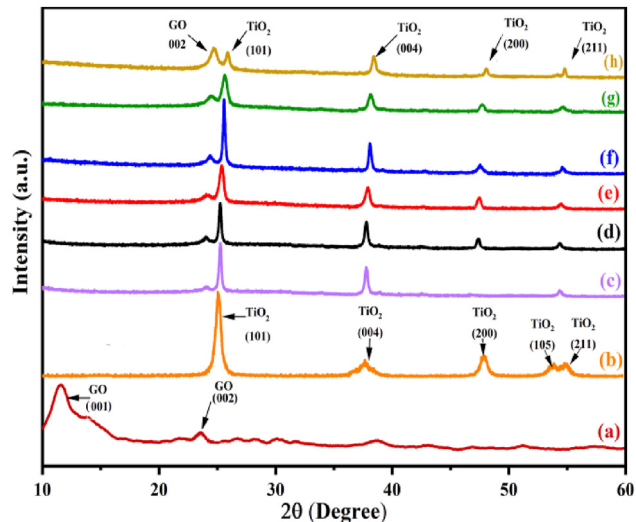

Fig. 2. X-ray diffraction of (a) GO, (b) TiO$_2$, (c) 0.5:4, (d) 1:4, (e) 2:4, (f) 3:4, (g) 4:4 and (h) 5:4 % GO:TiO$_2$-AD powders.

plane, which corresponds to the anatase phase of the TiO$_2$. The results depicted in Fig. 2 indicate disappears only the GO single diffraction peak at 11.7°, causing a clear peak at 24.21° from the (002) crystallographic plane. This implies that synthesis removes trapped within the material water. Additionally, van der Waals forces cause inter-sheet restacking. Additionally, the ultrathin nanosheet forms a conjugate network [23]. Crystallite size was estimated using the Scherrer formula [24].

$$D = \frac{0.94\lambda}{\beta \cos\theta} \qquad (1)$$

where β is the peak's full width at half maximum (FWHM) height, λ represents the incident wavelength of X-ray, and θ represents Bragg's diffraction angle. The crystallite sizes were found by taking the preferred (hkl) plane of GO (001) and (101) for TiO$_2$ and GO:TiO$_2$ powders. It was 4.46 nm for GO, 15.65 nm for TiO$_2$, 19.84, 19.38, 18.52, 17.32, 16.61, and 15.04 nm for GO:TiO$_2$ ratios of 0.5:4, 1:4, 2:4, 3:4, 4:4, and 5:4 respectively. The results show that increasing
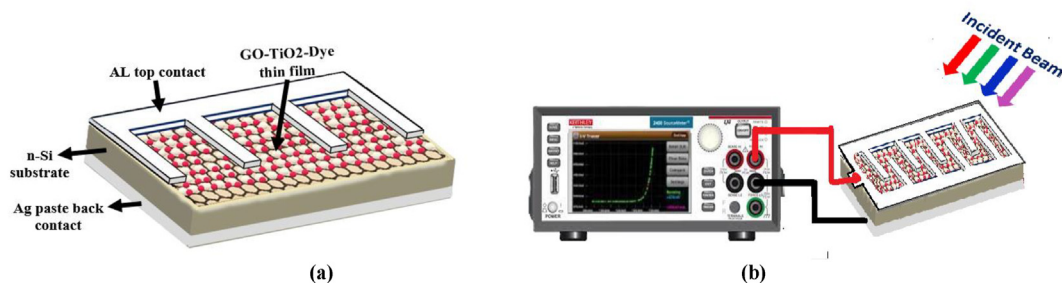

Fig. 1. (a) Schematics of a cross-section of one side from metal contact, (b) photodetector measurement circuit.

GO concentrations reduces crystallite size, which increases surface area and photodetectivity.

Figure 3 illustrates that GO:TiO$_2$-AD films have a surface morphology defined by several clusters or agglomerates randomly dispersed on the upper surface of the films. The TiO$_2$ nanoparticles were effectively deposited onto the GO plane, which exhibits a flat shape with slight creases. Because the TiO$_2$ nanoparticles tended to aggregate into large particles, the TiO$_2$ nanoparticles were well distributed on the GO nano-sheets [21].

The increment in GO concentration forms a continuous network with TiO$_2$, due to the conductance properties of graphene. This network is characterized by path wayes that facilitate the mobility of charge carriers, resulting in a low level of electrical resistance. Moreover, the agglomeration of TiO$_2$ enhance the photodetectivity activity by effectively separating the photogenerated charge pairs through inter-particle charge transfer inside the agglomerates [15,25].

3.2. Optical properties

Figure 4a exhibits the absorption spectra in the visible region of the GO:TiO$_2$ nanocomposite films immersed in anthocyanin dyesensitized. The films have distinctive absorbance at around 580 nm also at the range 400−800 nm. One can observe that the absorbance decreases with increasing wavelength from 300 to around 500 nm, while it increases with increasing GO ratio. On the other hand, the absorbance becomes constant for wavelengths more than 700 nm. The energy band gaps of prepared thin films can be determined by analyzing Tauc plot using Equation (2) [26].

$$\alpha h\nu = A(h\nu - E_g)^n \tag{2}$$

where α represents the absorption coefficient, A is the constant of proportionality, $h\upsilon$ is the incident energy, and E_g is the material's band gap. The prepared films have allowed a direct energy gap; the value of n is assumed to be 1/2. Consequently, Equation (2) can be expressed as

$$\alpha h\nu = A(h\nu - E_g)^{\frac{1}{2}} \tag{3}$$

Figure 4b depicts the relationship between the $(\alpha h\upsilon)^2$ and the photon energy of GO:TiO$_2$ −AD thin films. This data suggests that all films have direct energy gap characteristics. The addition of anthocyanin, a natural sensitizer, enhances the visible
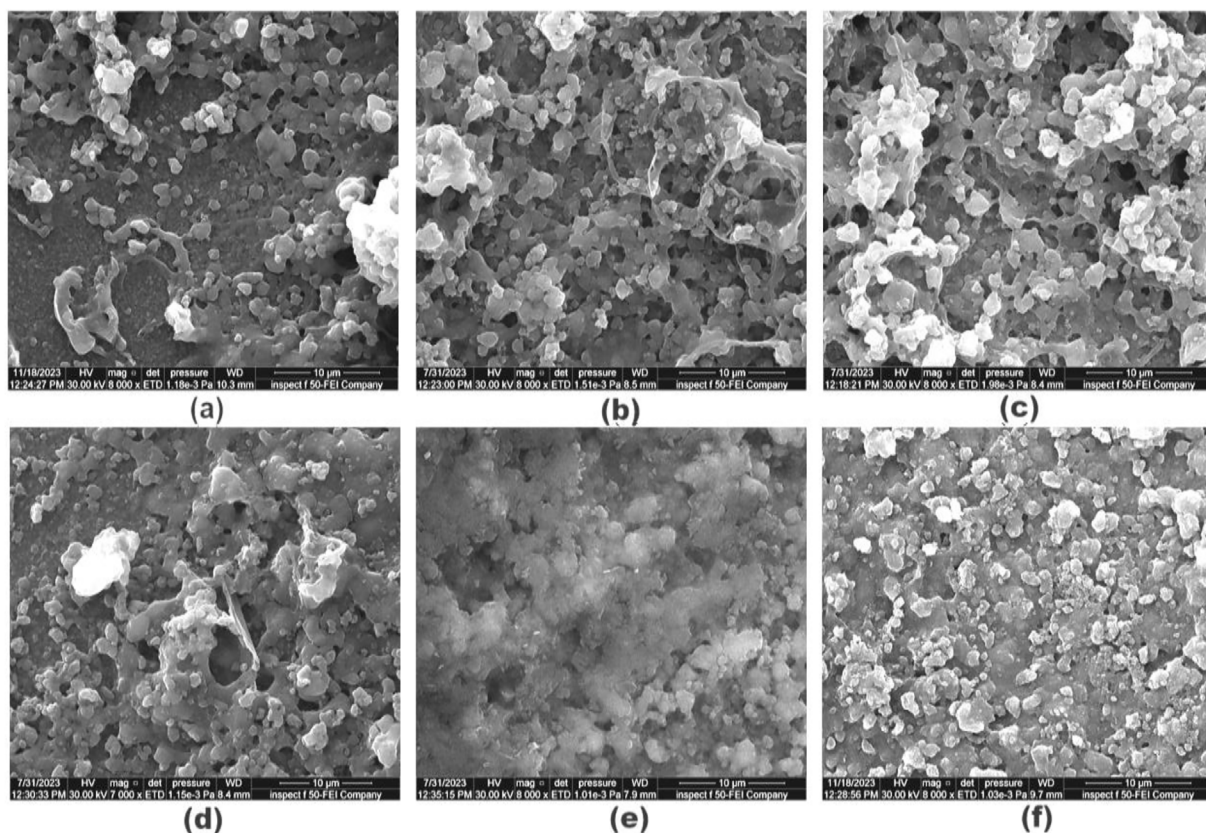

Fig. 3. . FESEM images of GO:TiO2-AD thin films at varies GO ratio% (a) 0.5:4; (b) 1:4; (c) 2:4; (d) 3:4; (e) 4:4; (f) 5:4.
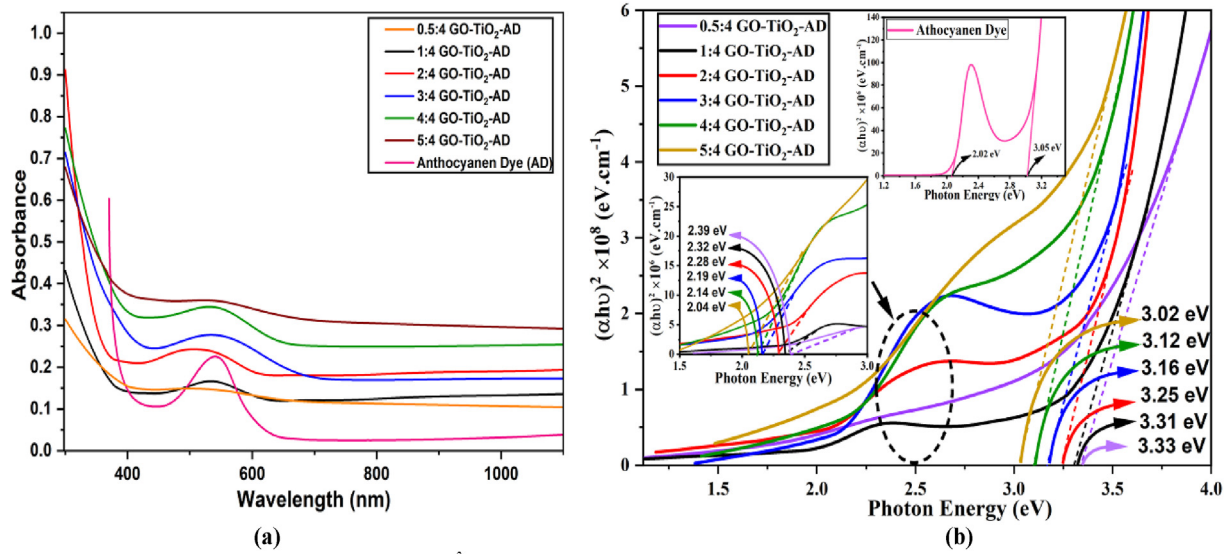
Fig. 4. (a) Absorbance spectra (b) Variation of $(\alpha h\nu)^2$ vs photon energy of $GO:TiO_2$-AD thin films, whereas the inset (a) Anthocyanin dye (b) the second energy gap.

region of the electromagnetic spectrum. Anthocyanins possess chromophore groups in its their chemical structure, allowing them to selectively absorb light within a specific range of the electromagnetic spectrum. The experimental results revealed the existence of two distinct energy gaps, one includes the ultraviolet wavelength due to π-π^* transitions of aromatic bonds C=C and n-π^* for transitions of aromatic bonds C=O corresponds to the range of visible wavelengths [27,28]. The value of the first energy gap viration between 3.33 and 3.02 eV, while the second energy gap have values 2.39 to 2.04 eV. Another significant change is that the GO concentration increase caused a reduction in the energy gap. This has significantly affected the photodetector characteristics of $GO:TiO_2$—AD thin films under visible light exposure [15].

3.3. Electrical properties

The ideality factor and barrier height values of the diodes were determined by analyzing the J-V characteristics using the thermionic emission mechanism, as described by the following Equations [29].

$$J_0 = A^* T^2 \exp\left(\frac{-q\varphi_b}{k_B T}\right) \qquad (4)$$

$$\varphi_b = \frac{k_B T}{q} \ln\left(\frac{A^* T^2}{J_0}\right) \qquad (5)$$

where φ_b the barrier height, J_0 is the saturation current density, k_B is the Boltzmann constant, T is

the absolute temperature and A* is the Richardson constant (A = 45.84 A/cm^{-2}K^{-2}) which is calculated from relation [30]:

$$A^* = \frac{(4\pi e m^* k_B^2)}{h^3} \approx 120 \frac{m^*}{m_0} \qquad (6)$$

where m* effective mass of GO and TiO_2 are $0.41m_0$ and $5.6m_0$, respectively. The value of the ideality factor, n, was calculated from the slope of the linear region of the forward bias ln(J)-V plot in Fig. 5 using the following relation [29]:
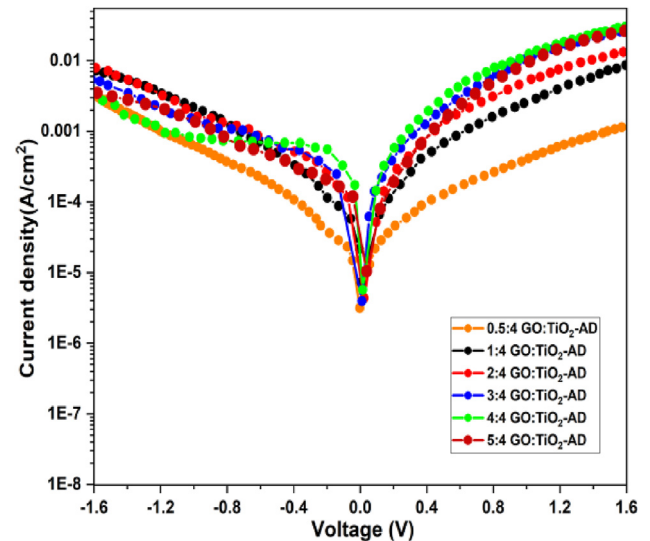

Fig. 5. The forward and reverse bias semi logarithmic J—V characteristics for GO:TiO2-AD/n-Si.

$$n = \frac{q}{k_{BT}}\left(\frac{dv}{dlnJ}\right) \tag{7}$$

The values of n obtained are significant, allowing for the analysis of the J-V characteristics of the diodes using the Cheung and Cheung technique [31]. This is due to the deviation of the ideality factor from the ideal value (n > 1), caused by both the series resistance and the non-uniform thickness of the films [32]. The series resistance is a crucial parameter that considerably impacts the electrical properties of Schottky barrier contacts. The interface layer between the metal and the semiconductor affects the resistance (R_s) and deviates from the ideal current density−voltage characteristics under forward bias. Barrier height (φ_b), ideality factor, and resistance (R_s) values are calculated using Equations [18]:

$$\left(\frac{dv}{dlnJ}\right) = \frac{nk_BT}{q} + JR_s \tag{8}$$

$$H(J) = V - \frac{nk_BT}{q}\ln\left(\frac{J}{A^*T^2}\right) \tag{9}$$

and H(J) is given by

$$H(J) = n\varphi_b + JR_s \tag{10}$$

The term JR_s in Equation (8) refers to the voltage drop across the series resistance of the device. The plots of dV/d(lnJ) and H(J) versus J for various GO ratio are displayed in Fig. 6. A plot in Fig. 6a shows dV/d(lnJ) versus J. The slope of the linear regression plot gives R_s. Simultaneously, nk_BT/q is the y-axis intercept from Equation (8).

The ideality factor derived from this method is lower than that obtained from the thermionic emission method due to the voltage drop across the series resistance.

Plotting the correlation between H(J) and J, as illustrated in Fig. 6b. The slope provides a different determination of R_s by employing the calculated ideality factor from Equation (5), the value of barrier height, φ_b, is determined from the y-axis intercept and Equation (10) [22]. This is relatively consistent with the barrier height in the thermionic emission model. Table 1 demonstrates the GO ratio's significant impact on reducing the leakage current density and ideality factor. The higher barrier height resulting from the numerous surface states on the nanostructured films can account for this decrease. The presence of surface states can be attributed to the higher concentration of oxygen vacancies and the anthocyanin dye layer. These surface states occur between the metal's native oxide layer and the contamination present at the metal−semiconductor interface. This implies that the barrier height may be regulated by choosing suitable interface materials, which is a significant benefit for the MOS junctions [33].

Figure 7 illustrates the relation between $1/C^2$ versus applied voltage at 1 MHz and 308 K. The linear relationship observed in the plot suggests an abrupt junction. The relationship between the slope of the plot and the effective carrier concentration N_d has been demonstrated, as indicated by Ref. [34].

$$N_d = -\left(\frac{2}{q\varepsilon_s\varepsilon_0 A^2}\right)\left[\frac{d(1/C^2)}{dv}\right]^{-1} \tag{11}$$

where ε_S and ε_o represent the relative permittivity of the semiconductor and vacuum, respectively, A is
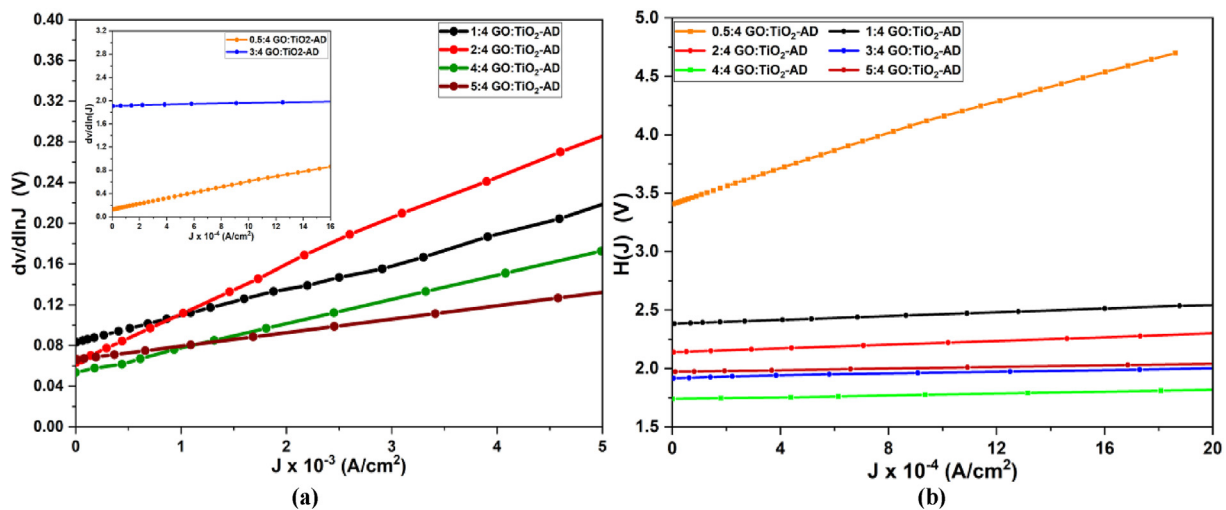

Fig. 6. Plot of (a) dv/dlnJ vs current density, (b) H(J) vs current density for GO:TiO$_2$-AD/n-Si.

Table 1. The values of n, R_s, Φ_b and J_s for GO: TiO_2-AD/n-Si.

GO:TiO_2-AD/nSi	J-V		Cheung				Js µA
	n	Φ_b eV	H(J)		dv/dlnJ		
			n	Φ_b eV	R_s $\Omega \cdot cm^{-2}$	R_s $\Omega \cdot cm^{-2}$	
0.5:4	4.8	0.70	4.7	0.68	707	462	9.8
1:4	3.1	0.72	3.1	0.70	662	653	8.9
2:4	2.7	0.73	2.6	0.71	67	41	5.93
3:4	2.4	0.75	2.3	0.73	40	39	3.96
4:4	2.2	0.77	2.1	0.75	36	30	3.21
5:4	2.6	0.71	2.6	0.70	42	38	9.17

the cross-section area of diode, the intersection of line $1/C^2$ with the x-axis represents the built-in voltage, V_{bi}. Based on the C–V plot, the curve intersecting the y-axis reveals the device's capacitance C_o. This value is obtained at zero bias, indicating the thickness of the depletion region W_d, calculated using the relation [35].

$$W_d = \frac{\varepsilon \varepsilon_0 A}{C_0} \qquad (12)$$

The C–V characteristics were used to determine the Φ_b, Fermi energy (E_F), effective density of states (N_c) for electrons in the semiconductor conduction bands (E_C). The image force lowering of barrier height and E_{max} using the following relations [34,35]:

$$\varphi_b(c-v) = V_{bi} + \frac{k_B T}{q} + E_F - \Delta\varphi_b \qquad (13)$$

$$E_F = \frac{k_B T}{q}\left(\frac{N_c}{N_d}\right) \qquad (14)$$

Fig. 7. The reverse bias ($1/C^2$–V) and C–V plot (in the inset) of GO:TiO_2-AD/n-Si.

$$N_c = 4.82 \times 10^{15} T^{\frac{3}{2}}\left(\frac{m_e^*}{m_0}\right)^{\frac{3}{2}} \qquad (15)$$

$$\Delta\varphi_b = \left[\frac{qE_{max}}{4\pi\varepsilon_0\varepsilon}\right]^{\frac{1}{2}} \qquad (16)$$

$$E_{max} = \frac{2V_{bi}}{W_d} \qquad (17)$$

The calculated values are listed in Table 2. V_{bi}, E_F, and φ_b values rise as the GO ratio increases. However, the values of N_d and $\Delta\varphi_b$ showed declinations except for 5% GO. Additionally, it has been noted that the barrier height increases as the image force barrier decreases. The photodiode's (C–V) characteristic exhibits the p-n junction's typical behavior. The capacitance exhibited a rapid declination as the reverse voltage increased, owing to the widening of the depletion layer in the heterojunction. A growth in the depletion layer width could be advantageous for enhancing photosensitivity and improving response speed. Based on the aforementioned experimental findings, Fig. 8 depicts the schematic energy band diagram for the heterojunction at zero bias. The dye was adsorbed onto TiO_2 molecules through chelation, creating a Ti–O–C link. It is connected to GO sheets through π–π* stacking through the carboxyl group, which possesses hole transfer capabilities [36]. When the GO: TiO_2 composite is applied to silicon, it equilibrates the Fermi energy. Under thermal equilibrium conditions, electron and hole diffusion and drift create a depletion zone at the interface, resulting from a positively charged Si site with a negatively charged TiO_2 at the GO:TiO_2/n-Si junction. This creates an inherent, integrated electric field that persists without external influence in the self-powered photodetector.

Furthermore, Anthocyanin dye is inserted between GO:TiO_2 nanocomposites and Si, altering the energy band structure. GO possesses several characteristics, including nuclei, bonded chemical entities, and an elongated π-π* configuration of carbon atoms, allowing for manipulating surface
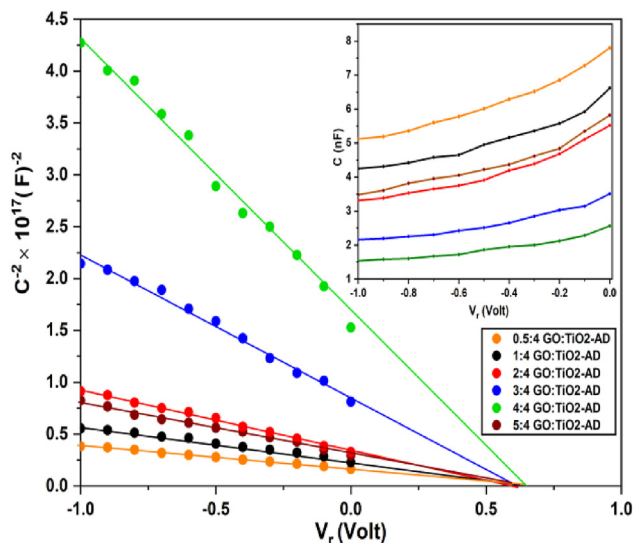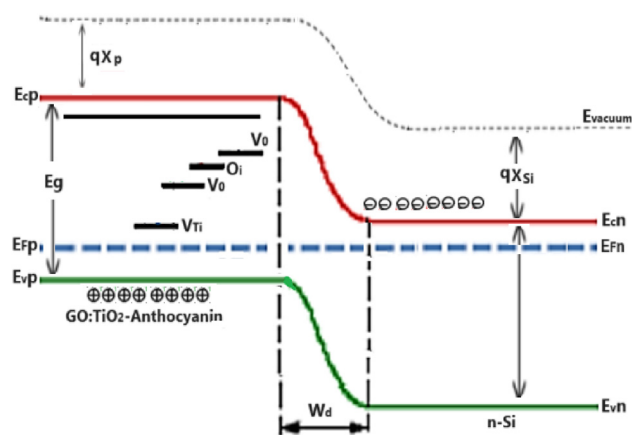
Table 2. The electrical parameters from ($1/C^2-V$) characteristics for GO:TiO$_2$-AD/n-Si.

GO:TiO$_2$-AD	C_0 nF	V_{bi} Volt	N_d $\times 10^{16}$ cm^{-3}	$E_{max}\times10^4$ V/m	W_d nm	E_F eV	Φ_b eV	$\Delta\Phi_b$ meV
0.5:4	7.80	0.67	2.74	8.36	160	0.14	0.83	1.09
1:4	6.62	0.52	1.44	6.49	160	0.16	0.70	0.84
2:4	5.52	0.57	1.15	6.49	175	0.16	0.76	0.84
3:4	3.52	0.59	0.473	3.96	297	0.19	0.80	0.51
4:4	2.56	0.61	0.249	3.22	378	0.20	0.84	0.41
5:4	5.82	0.61	1.21	6.27	194	0.17	0.80	0.81

Fig. 8. Schematic energy band diagrams for the heterojunction at zero bias of GO:TiO$_2$-AD/n-Si.

states and intrinsic emissions. The interaction between GO sheets, TiO$_2$ defect centers, and anthocyanin dye creates chemical bonds and a boundary effect, creating sublevels (traps) that facilitate electron transitions; the interface trap charges substantially impact the improvement of photocurrent and lead to novel characteristics in the detection behavior [37]. Following exposure to visible irradiation, anthocyanin molecules absorb light, generating electron−hole pairs (excitons) that migrate to the interface between anthocyanin and the TiO$_2$ layer. GO enhances electron transfer efficiency due to its electrical properties and large surface area, potentially facilitating charge transport between the layers. The transferred electrons in the TiO$_2$ layer move toward the electrode, while the holes in the anthocyanin layer move toward the n-Si substrate. This movement creates a potential difference across the heterojunction. Fig. 9 depicts the shifts in the conduction band sublevels induced by the GO sheet toward the valence band of TiO$_2$.

Titanium dioxide absorbs ultraviolet (UV) light at a wavelength of 380 nm in its valence band. Absorbs blue light with a wavelength of 460 nm through the GO:TiO$_2$-AD nanocomposite when the sp^2 clusters move from being alone to joining with the sp^3 C−O matrix. The defects and vacancy concentration have increased transitions from the conduction band to

the valence band, particularly from V.B. (C. B→O$_i$, →V$_{Ti}$, V$_O$→V.B, and O$_i$). These transitions are linked to the absorption of wavelengths between 520 and 620 nm [38,39].

3.4. Photodetector properties

Figure 10(a-d) display the photodetector device's current versus time (I-t) graph. The device was tested at wavelengths of 380, 460, 520, and 620 nm, with power intensities of 6.17, 5.61, 10.38, and 5.11 mW/cm^2, respectively. These tests were conducted without applying any bias voltage. The gadget demonstrated consistent current during multiple cycles, displaying excellent repeatability and stability. The photodetector's rise time (τ_{Rise}) is the duration for the photocurrent to reach 90% of its maximum value, starting from its initial dark current value. The photodetector's decay time (τ_{Decay}) refers to the duration it takes for the photodetector's dark current value decrease to 10% of its initial photocurrent value [40]. Photoresponsivity (R_λ) refers to the ratio between the output electrical signal and the incident optical power at a specific wavelength [41].

$$R_\lambda = \frac{I_{photo}}{P_{in}S} \tag{18}$$
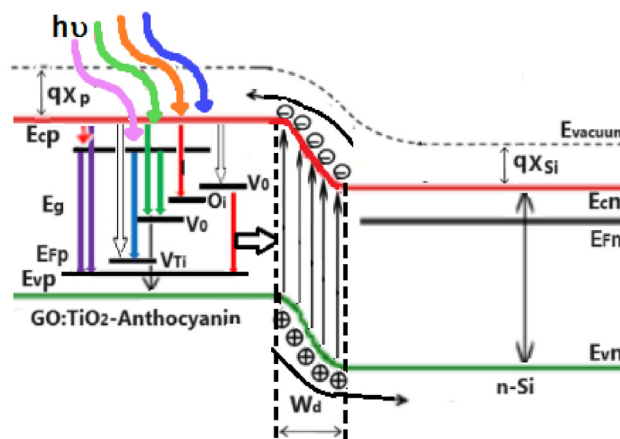
Fig. 9. Schematic energy band diagrams under illumination for GO:TiO$_2$-AD/n-Si heterojunction.
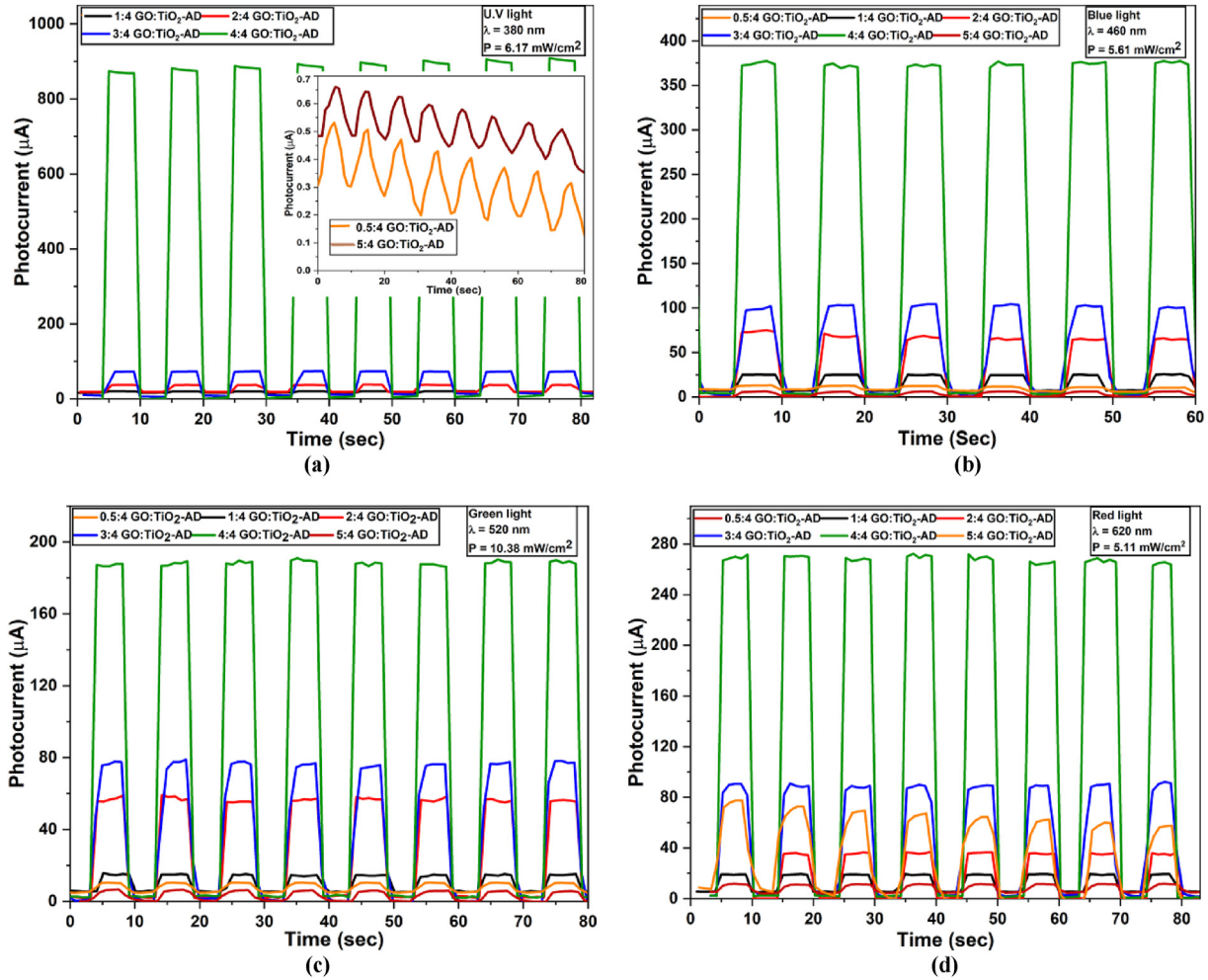
Fig. 10. The variation of photocurrent with time for GO: TiO_2-AD/n-Si self-power photodetectors (SPPDs) under various wavelengths and light intensities (a) 380 nm with 6.17 mW/cm^2 (b) 460 nm with 5.61 mW/cm^2 (c) 520 nm with 10.38 mW/cm^2 (d) 620 nm with 5.11 mW/cm^2.

The generated photocurrent is denoted as I_{photo}, the active area of the photodetector is represented by S, and the strength of incident radiation or light is indicated as P_{in}. External quantum efficiency (η) refers to the ratio of the number of charge carriers a device generates to the number of photons incident on the device. It provides insight into the efficacy of photodetectors in converting photons into distinct charge carriers. The term refers to the proportion of holes or electrons that are transformed through the stimulation of photons by an energy source. The evaluation is conducted by employing the following Equations [39,41]:

$$EQE(\eta) = \frac{I_{photo}}{P_{in}S} \times \frac{hc}{q\lambda} \times 100\% \tag{19}$$

$$EQE(\eta) = R \times \frac{hc}{q\lambda} \times 100\% \tag{20}$$

where h represents the Planck constant, c represents the velocity of light, and q is the unit of electric charge. Photosensitivity (ξ) refers to the variation in current about the dark current. The photosensitivity is the quotient of the change in current (ΔI) divided by the dark current [42].

$$\xi = \frac{I_{photo} - I_{dark}}{I_{dark}} \tag{21}$$

Specific detectivity (D*) of photodetector refers to its capacity to detect low-intensity signals given by Ref. [43]:

$$D^* = \frac{\sqrt{Sf}}{NEP} \qquad (22)$$

where f is the bandwidth, the acronym NEP stands for noise equivalent power. It is appraised.

$$NEP = \frac{i_n}{R} \qquad (23)$$

where i_n represents the dark current noise. Fig. 11(a-d) shows the values of photosensitivity (ξ), responsivity (R_λ), noise equivalent power(NEP) and specific detectivity (D*) versus wavelengths of GO:TiO$_2$-AD/n-Si thin films. Table 3 illustrates that the most significant values of ξ, R_λ, η, NEP, D* and rise time (τ_{Rise}) of the GO:TiO$_2$-AD/n-Si photodetector were evaluated at concentration 4:4 GO:TiO$_2$-AD/n-Si at wavelength 380 nm to be 8851, 0.96 A·W^{-1}, 305.5%, 8.39×10^{-13} W·Hz$^{-1/2}$,

3.06×10^{11} Jones and 0.79 s respectively, indicating the detection ability of the GO:TiO$_2$-AD/n-Si SPPDs. These values are closed to that published in SPPDs literatures [44−48].

EQE slightly decreases at wavelength 520 nm, possibly due to the loss of high energy photons at the heterojunction surface. The high concentration of GO may be useless as it may reduce the external quantum efficiency and responsivity of the device, as noted at concentration 5:4 GO:TiO$_2$-AD/n-Si. This may be attributed to the photo desorption of oxygen on the GO:TiO$_2$-AD surface, leading to a reduction in the photocurrent. The oxygen molecules act as electron acceptors and confer p-type doping on GO [49], so the conductivity will decrease when oxygen is desorbed from the GO:TiO$_2$-AD surface under illumination.
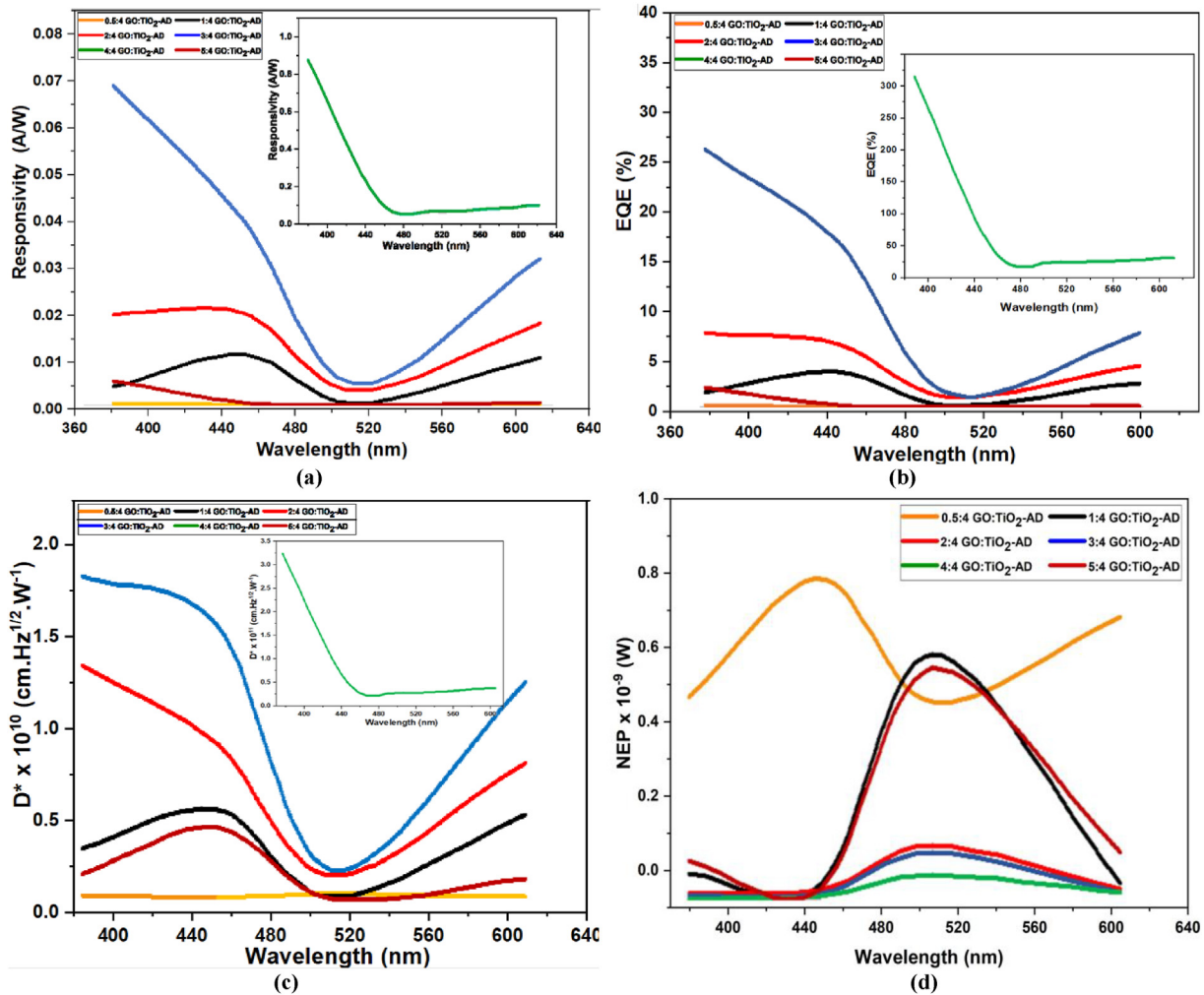

Fig. 11. Variation of (a) photoresponsivity vs wavelength (b) EQE vs wavelength (c) D* vs wavelength (d) NEP vs wavelength for GO: TiO$_2$- AD/n-Si self-power photodetectors (SPPDs).

Table 3. The values of ξ, R_λ, η, NEP and D* of GO: TiO₂-AD/n-Si self-power photodetectors (SPPDs).

GO:TiO₂-AD/n-Si	ξ %	$R_\lambda \times 10^{-3}$ A/W	η %	NEP $\times 10^{-11}$ W·Hz$^{1/2}$	D* $\times 10^{9}$ (Jones)	τ_{Rise} sec
U.V light (380 nm)						
0.50%	532	0.57	0.18	55.79	0.44	0.85
1%	1544	4.47	1.42	7.08	3.49	0.85
2%	3918	21.86	6.94	1.62	15.23	0.85
3%	2486	76.59	24.35	1.22	20.94	0.85
4%	8851	961.00	305.5	0.08	305.89	0.79
5%	1666	5.72	1.82	10.6	1.83	1.4
Green light (520 nm)						
0.50%	1177	0.04	0.009	54.63	0.50	0.69
1%	273	0.79	0.188	67.79	0.38	0.78
2%	2365	3.72	0.886	14.64	1.71	0.83
3%	744	5.13	1.222	13.01	2.06	0.72
4%	5231	12.15	2.898	6.54	3.87	0.81
5%	385	0.04	0.009	63.80	0.24	2.24
Blue light (460 nm)						
0.50%	324	0.08	0.02	88.59	0.27	0.92
1%	1877	12.30	3.31	4.16	5.97	0.85
2%	1488	22.09	5.95	2.51	10.15	0.8
3%	755	44.28	15.6	1.45	17.75	0.78
4%	2495	82.74	22.3	0.99	26.34	0.76
5%	2021	0.83	0.22	3.14	4.82	2.3
Red light(620 nm)						
0.50%	2830	0.10	0.01	77.98	0.32	0.83
1%	2740	11.64	2.32	4.59	5.62	0.78
2%	766	19.66	3.93	2.84	9.04	0.79
3%	8480	35.02	7.00	1.84	14.11	0.78
4%	13,300	47.37	9.47	1.73	15.15	0.76
5%	2910	0.90	0.18	13.20	1.56	1.24

4. Conclusions

The GO: TiO₂-AD/n-Si photodetectors synthesized successfully with different concentrations of GO have been deposited using a spray pyrolysis deposition technique. Through XRD examinations, the polycrystalline structure of GO: TiO₂ films with anatase phase were confirmed. The crystallite sizes were decreased with increasing GO concentration. The morphology for films has several agglomerates randomly dispersed on the upper surface of the films. As the GO concentration increases, a continuous network with TiO₂ forms. The data reveals that all films have allowed direct energy gap which are decreased with increasing the GO concentration. The type of junction is abrupt. The width of depletion layer and φ_b increase with increasing GO concentration from 1 to 4%, whereas the N_d decreases. The increment of GO concentration caused increase in photoresponsivity, photosensitivity and specific detectivity for various wavelength. The prepared detector for 4: 4 GO: TiO₂-AD/n-Si concentration has greatest values for figure of merit. This study presents a rapid response multi photodetector with low noise constructed using a GO:TiO₂-AD/n-Si heterostructure. The demonstrated effective charge separation capabilities, responsivity, and sensitivity make this heterostructure an exciting choice for detector applications. These results are promising for the development of next generation optoelectronic devices, such as hybrid or dye sensitized solar cells, ultraviolet and visible detectors.

Acknowledgment

References

[1] P. Deb, J.C. Dhar, Enhanced absorption and Photo- emission from TiO₂ nanowire/graphene oxide thin film hetero structure, J. Electron. Mater. 47 (2018) 6078−6085, https://doi.org/10.1007/s11664-018-6503-3.

[2] A. Al-Shawi, M. Alias, P. Sayers, M.F. Mabrook, Improved memory properties of graphene oxide-based organic memory transistors, Micromachines 10 (2019) 643, https://doi.org/10.3390/mi10100643.

[3] S.K. Behura, C. Wang, Y. Wen, V. Berry, Graphene−semiconductor heterojunction sheds light on emerging photovoltaics, Nat. Photonics. 13 (2019) 312−318, https://doi.org/10.1038/s41566-019-0391-9.

[4] L. Guo, Y.W. Hao, P.L. Li, J.F. Song, R.Z. Yang, X.Y. Fu, S.Y. Xie, J. Zhao, Y.L. Zhang, Improved NO₂ gas sensing properties of graphene oxide reduced by two beam laser interference, Sci. Rep. 8 (2018) 4918, https://doi.org/10.1038/s41598-018-23091-1.

[5] F. Zhao, J. Liu, X. Huang, X. Zou, G. Lu, P. Sun, S. Wu, W. Ai, M. Yi, X. Qi, L. Xie, J. Wang, H. Zhang, W. Huang, Chemo-selective photodeoxidization of graphene oxide using steri-cally hindered amines as catalyst: synthesis and applications, ACS Nano 6 (2012) 3027–3033, https://doi.org/10.1021/nn2047185.

[6] D. Nunes, A. Pimentel, A. Araujo, T.R. Calmeiro, S. Panigrahi, J.V. Pinto, P. Barquinha, M. Gama, E. Fortunato, R. Martins, Enhanced uv flexible photo detectors and pho-tocatalysts based on TiO$_2$ nano- platforms, Top Catal. 61 (2018) 1591–1606, https://doi.org/10.1007/s11244-018-0968-4.

[7] A.M.A. Hussein, S.A. Abdullah, M. Rasheed, R.S. Zamel, Optical and electrical properties of glass/graphene oxide thin films, Iraq. J. Phy. 18 (2020) 73–83, https://doi.org/10.30723/ijp.v18i47.617.

[8] L.S. Chougala, M.S. Yatnatti, R.K. Linganagoudar, R.R. Kamble, J.S. Kadadevarmath, A simple approach on synthesis of TiO$_2$ nanoparticles and its application in dye sensitized solar cells, J. Nano Electron. Phys. 9 (2017) 4005–4006, https://doi.org/10.21272/jnep.9(4).04005.

[9] L.I. Mohi, A.F. Abdulameer, Optical investigation of reduced graphene oxide/titanium dioxide nanocomposite thin films synthesized by hydrothermal method, Iraq. J. Phy. 22 (2024) 75–81, https://doi.org/10.30723/ijp.v22i1.1197.

[10] I. Sta, M. Jlassi, M. Hajji, M.F. Boujmil, R. Jerbi, M. Kandyla, M. Kompitsas, H. Ezzaouia, Structural and optical properties of TiO$_2$ thin films prepared by spin coating, J. Sol. Gel. Sci. Technol. 72 (2014) 421–427, https://doi.org/10.1007/s10971-014-3452-z.

[11] P. Deb, J.C. Dhar, Fast response uv photodetection using TiO$_2$ nanowire/graphene oxide thin-film Heterostructure, IEEE Photonics. Technol. Lett. 31 (2019) 571–574, https://doi.org/10.1109/lpt.2019.2900283.

[12] S.A. Bhandarkar, Prathvi, A. Kompa, M.S. Murari, D. Kekuda, R.K. Mohan, Investigation of structural and optical properties of spin coated TiO$_2$: Mn thin films, Opti. Mat. 118 (2021) 111254, https://doi.org/10.1016/j.optmat.2021.111254.

[13] V. Štengl, S. Bakardjieva, T.M. Grygar, J. Bludská, M. Kormunda, TiO$_2$-graphene oxide nano composite as advanced photocatalytic materials, Chem. Cent. J. 7 (2013) 1–12, https://doi.org/10.1186/1752-153x-7-41.

[14] S.D. Al-Algawi, R.T. Rasheed, Z.R. Rhoomi, Structural and optical properties of annealed TiO$_2$ powder synthesized by hydrothermal method, Iraq. J. Phy. 58 (2017) 1683–1693, https://ijs.uobaghdad.edu.iq/index.php/eijs/article/view/5798.

[15] W. Vallejo, A. Rueda, C.D. Uribe, C. Grande, P. Quintana, Photocatalytic activity of graphene oxide TiO$_2$ thin films sensitized by natural dyes extracted from bactris guineensis, R. Soc. Open Sci. 6 (2019) 181824, https://doi.org/10.1098/rsos.181824.

[16] N.J. Cherepy, G.P. Smestad, M. Grätzel, Jin Z. Zhang, Ul-trafast electron injection: implications for a photo-electrochemical cell utilizing an anthocyanin dye-Sensitized TiO$_2$ nanocrystalline electrode, J. Phys. Chem. B 101 (1997) 9342–9351, https://doi.org/10.1021/jp972197w.

[17] Q. Dai, J. Rabani, Photosensitization of nanocrystalline TiO$_2$ films by anthocyanin dyes, J. Photochem. Photobio. A:Chem. 148 (2002) 17–24, https://doi.org/10.1016/s1010-6030(02)00073-4.

[18] A.H. Ahliha, F. Nurosyid, A. Supriyanto, T. Kusumaningsih, Optical properties of anthocyanin dyes on TiO$_2$ as photo-sensitizers for application of dye-sensitized solar cell (DSSC), IOP Conf. Ser. Mater. Sci. Eng. 333 (2018) 012018, https://doi.org/10.1088/1757-899x/333/1/012018.

[19] N. Gokilamani, N. Muthukumarasamy, M. Thambidurai, A. Ranjitha, D. Velauthapillai, Utilization of natural antho-cyanin pigments as photosensitizers for dye sensitized solar cells, J. Sol. Gel. Sci. Technol. 66 (2013) 212–219, https://doi.org/10.1007/s10971-013-2994-9.

[20] B. Enaru, G. Drețcanu, T.D. Pop, A. Stănilă, Z. Diaconeasa, Anthocyanins: factors affecting their stability and degrada-tion, Antioxidants 10 (2021) 1967, https://doi.org/10.3390/antiox10121967.

[21] J. Qiu, C. Lai, Y. Wang, S. Li, S. Zhang, Resilient mesoporous TiO$_2$/graphene nanocomposite for high rate performance lithium-ion batteries, Chem. Eng. J. 256 (2014) 247–254, https://doi.org/10.1016/j.cej.2014.06.116.

[22] S. Jamil, M. Fasehullah, Effect of temperature on structure, morphology, and optical properties of TiO$_2$ nanoparticles, Mater. Inn. 1 (2021) 22–28, https://doi.org/10.54738/mi.2021.1103.

[23] Y.-C. Wang, C.-P. Cho, Application of TiO$_2$- graphene nanocomposites to photoanode of dye- sensitized solar cell, J. Photochem. Photobi. A 332 (2017) 1–9, https://doi.org/10.1016/j.jphotochem.2016.07.036.

[24] B.D. Cullity, Elements of X Ray diffraction, in: Franklin Classics, second ed., 2018.

[25] J. Song, X. Wang, C.T. Chang, Preparation and character-ization of graphene oxide, J. Nanomater. 2014 (2014) 1–6, https://doi.org/10.1155/2014/276143.

[26] M. Yõldõrõm, Characterization of the framework of Cu doped TiO$_2$ layers: an insight into optical, electrical and photodiode parameters, J. All. Comp. 773 (2019) 890–904, https://doi.org/10.1016/j.jallcom.2018.09.276.

[27] A. Carissa, M.S. Esteban, E.P. Enriquez, Graphene- antho-cyanin mixture as photosensitizer for dye sensitized solar cell, Sol. Energy 98 (2013) 392–399, https://doi.org/10.1016/j.solener.2013.09.036.

[28] X. Zhang, H.P. Li, X. Cui, Y. Lin, Graphene/TiO$_2$ nano-composites: synthesis, characterization and application in hydrogen evolution from water photo- catalytic splitting, J. Mater. Chem. 20 (2010) 2801–2806, https://doi.org/10.1039/b917240h.

[29] E.H. Rhoderick, R.H. Williams, Metal Semiconductor Con-tacts, second ed., Clarendon, Oxford. 1988.

[30] C.A. Amorim, E.P. Bernardo, E.R. Leite, A.J. Chiquito, Effect of inhomogeneous Schottky barrier height of SnO$_2$ nano-wires device, Semicond. Sci. Technol. 33 (2018) 055003, https://doi.org/10.1088/1361-6641/aab69e.

[31] S.K. Cheung, N.W. Cheung, Extraction of Schottky diode parameters from forward current-voltage characteristics, Appl. Phys. Lett. 49 (1986) 85–87, https://doi.org/10.1063/1.97359.

[32] H.M. Al-Ta'ii, V. Periasamy, Y.M. Amin, Electronic charac-terization of Au/DNA/ITO metal -semiconductor metal diode and its application as a radiation sensor, PLoS One 11 (2016) 1–17, https://doi.org/10.1371/journal.pone.0145423.

[33] F. Esra, C. Çatõr, The structural, optical, and electrical characterization of Ti/n InP Schottky diodes with graphene oxide interlayer deposited by spray pyrolysis method, Phys. Status Solidi. 217 (2020) 2000125, https://doi.org/10.1002/pssa.202000125.

[34] S.M. Sze, Physics of Semiconductor Devices, second ed., Wiley, New York. 1981.

[35] E.H. Nicollian, J.R. Brews, MOS (Metal/Oxide/Semi-conductor) Physics and Technology, Wiley, New York. 1982.

[36] A.A. Hendi, F. Yakuphanoglu, Graphene doped TiO$_2$/p-sili-con heterojunction photodiode, J. All. Com. 665 (2016) 418–427, https://doi.org/10.1016/j.jallcom.2016.01.045.

[37] T. Ji, Q. Liu, R. Zou, Y. Sun, K. Xu, L. Sang, M. Liao, Y. Koide, L. Yu, J. Hu, An interface engineered multicolor photode-tector based on n-Si(111)/TiO$_2$ nanorod array heterojunction, Adv. Funct. Mater. 26 (2016) 1400–1410, https://doi.org/10.1002/adfm.201504464.

[38] G. Eda, Y.Y. Lin, C. Mattevi, H. Yamaguchi, H.A. Chen, I.S. Chen, C.W. Chen, M. Chhowalla, Blue photo- lumines-cence from chemically derived graphene oxide, Adv. Mater. 22 (2010) 505–509, https://doi.org/10.1002/adma.200901996.

[39] N. Huo, G. Konstantatos, Recent progress and future pros-pects of 2D based photodetectors, Adv. Mater. 30 (2018) 1801164, https://doi.org/10.1002/adma.201801164.

[40] N.K.R. Nallabala, S.V.P. Vattikuti, V.K. Verma, V.R. Singh, S. Alhammadi, V.K. Kummara, V. Manjunath, M. Dhanalakshmi, V.R.M. Reddy, Highly sensitive and cost-effective metal- semiconductor-metal asymmetric type Schottky metallization based ultraviolet photo- detecting

sensors fabricated on n-type GaN, Mater. Sci. Semicond. Process 138 (2022) 106297, https://doi.org/10.1016/j.mssp.2021.106297.

[41] A.L. Punde, S.P. Shah, Y.V. Hase, A.D. Waghmare, P.S. Shinde, B.R. Bade, H.M. Pathan, M. Prasad, S.P. Patole, S. Jadkar, Self-biased photodetector using 2D layered bismuth triiodide (BiI_3) prepared using the spin coating method, RSC Adv. 12 (2022) 30157−30166, https://doi.org/10.1039/d2ra05484a.

[42] G.X. Liang, C.H. Li, J. Zhao, Y. Fu, Z.X. Yu, Z.H. Zheng, Z.H. Su, P. Fan, X.H. Zhang, J.T. Luo, L. Ding, S. Chen, Self-powered broadband kesterite photodetector with ultrahigh specific detectivity for weak light applications, SusMat 3 (2023) 682−696, https://doi.org/10.1002/sus2.160.

[43] D. Hao, D. Liu, Y. Shen, Q. Shi, J. Huang, Air stable self-powered photodetectors based on lead free $CsBi_3I_{10}/SnO_2$ heterojunction for weak light detection, Adv. Funct. Mater. 31 (2021) 1−9, https://doi.org/10.1002/adfm.202100773.

[44] T.-F. Zhang, Z.-P. Li, J.-Z. Wang, W.-Y. Kong, G.-A. Wu, Y.-Z. Zheng, Y.-W. Zhao, E.-X. Yao, N.-X. Zhuang, L.-B. Luo, Broadband photodetector based on carbon nanotube thin film single/layer graphene Schottky junction, Sci. Rep. 6 (2016), https://doi.org/10.1038/srep38569.

[45] J. Xu, W. Yang, H. Chen, L. Zheng, M. Hu, Y. Li, X. Fang, Efficiency enhancement of TiO_2 self-powered UV photodetectors using a transparent Ag nanowire electrode, J. Mater. Chem. C 6 (2018) 3334−3340, https://doi.org/10.1039/c8tc00550h.

[46] M. Kumar, J.-Y. Park, H. Seo, High-Performance and self-powered alternating current ultraviolet photodetector for digital communication, ACS Appl. Mater. Interfaces 13 (2021) 12241−12249, https://doi.org/10.1021/acsami.1c00698.

[47] T. Yan, S. Cai, Z. Hu, Z. Li, X. Fang, Ultrafast speed, dark current suppression, and self-powered enhancement in TiO_2-based ultraviolet photodetectors by organic layers and Ag nanowires regulation, J. Phys. Chem. Lett. 12 (2021) 9912−9918, https://doi.org/10.1021/acs.jpclett.1c03090.

[48] Z. Zhou, X. Li, F. Zhao, C. Wang, M. Zhang, S. He, Y. Zhang, D. Zhang, M. Xu, L. Zhang, Self-powered heterojunction photodetector based on thermal evaporated p-CuI and hydrothermal synthesised n-TiO_2 nanorods, Opt. Mater. Express 12 (2022) 392, https://doi.org/10.1364/ome.448435.

[49] D.T. Phan, G.S. Chung, P−n junction characteristics of graphene oxide and reduced graphene oxide on n-type Si(111), J. Phys. Chem. Solid. 74 (2013) 1509−1514, https://doi.org/10.1016/j.jpcs.2013.02.007.